

## Analysis of improved digital filter inflow generation methods for compressible turbulent boundary layers

Laguarda, Luis; Hickel, Stefan

**DOI**

[10.1016/j.compfluid.2023.106105](https://doi.org/10.1016/j.compfluid.2023.106105)

**Publication date**

2024

**Document Version**

Final published version

**Published in**

Computers and Fluids

**Citation (APA)**

Laguarda, L., & Hickel, S. (2024). Analysis of improved digital filter inflow generation methods for compressible turbulent boundary layers. *Computers and Fluids*, 268, Article 106105. <https://doi.org/10.1016/j.compfluid.2023.106105>

**Important note**

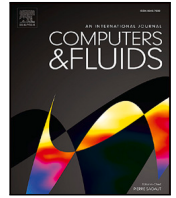
To cite this publication, please use the final published version (if applicable). Please check the document version above.

**Copyright**

Other than for strictly personal use, it is not permitted to download, forward or distribute the text or part of it, without the consent of the author(s) and/or copyright holder(s), unless the work is under an open content license such as Creative Commons.

**Takedown policy**

Please contact us and provide details if you believe this document breaches copyrights. We will remove access to the work immediately and investigate your claim.



# Analysis of improved digital filter inflow generation methods for compressible turbulent boundary layers

Luis Laguarda, Stefan Hickel\*

Department of Flow Physics and Technology, Faculty of Aerospace Engineering, Technische Universiteit Delft, Kluyverweg 1, 2629 HS Delft, The Netherlands

## ARTICLE INFO

### Keywords:

Turbulence resolving simulation  
Turbulent inflow generation  
Digital filter

## ABSTRACT

We propose several enhancements to improve the accuracy and performance of the digital filter turbulent inflow generation technique and assess their efficacy in the context of wall-resolved large-eddy simulations of a compressible turbulent boundary layer. Improvements of accuracy include a more realistic correlation function for the transversal directions, target length scales that vary with wall-distance, and a counter-intuitive approach that involves the suppression of streamwise velocity fluctuations at the inflow. For improving the computational performance, we propose to generate the inflow data in parallel in single precision and at a prescribed time interval based on the turbulence time scale, and not at every time-step of the simulation. Based on the results of 7 wall-resolved large-eddy simulations, we find that the new correlation functions and the considered performance improvements are beneficial and therefore desired. Suppressing streamwise velocity fluctuations at the inflow leads to the fastest relaxation of the pressure fluctuations; however, this approach increases the adaptation length defined in terms of compliance with the von Kármán integral equation. The adaptation length can be shortened by artificially increasing the wall-normal Reynolds stresses, thereby preserving the desired turbulence kinetic energy level. A detailed inspection of the Reynolds stress transport budgets reveals that the observed spurious spatial transients are largely driven by pressure-related terms. For instance, increased values of  $\overline{u'p'}$  are found throughout the computational domain when a physical Reynolds stress distribution is prescribed at the inflow. Therefore, efforts to enhance digital filter techniques should aim at modeling pressure fluctuations as well as their correlation with the velocity components.

## 1. Introduction

Turbulence-resolving simulations, such as direct and large-eddy simulations (DNS and LES) provide the highest accuracy for the study of complex phenomena in wall-bounded turbulence and associated flow-control applications. However, quality and reliability of the resulting data strongly depends on the accuracy of the employed boundary conditions. Of particular relevance is the inflow boundary condition, which dictates the downstream flow evolution. Inappropriate inflow data can lead to excessively long spatial transients until the turbulent flow is fully developed. This naturally increases the computational domain size required for a given flow problem, which, in the worst case, can become intractable in combination with the high spatio-temporal resolution requirements of LES and DNS.

For these reasons, a vast variety of turbulence generation methodologies have emerged in the past decades [1–3]. Besides data-driven approaches, where the inflow condition stems from a detailed data base, a reduced-order model of the same flow [4] or, more recently, from deep learning models [5], turbulence generation techniques are

classified into recycling methods and synthetic methods. Recycling methods extract the required inflow state from an auxiliary simulation or directly from a downstream plane with appropriate re-scaling [6,7]. Synthetic inflow methods, on the other hand, are based on constraining random fluctuations to satisfy prescribed statistics and recover a target coherence or energy spectrum [8–10]. Comprehensive reviews of the available techniques within these two categories are provided by Tabor and Baba-Ahmadi [1], Wu [2] and Dhamankar et al. [3].

An example for synthetic turbulence generation methods is the so-called digital filter technique [9,11]. This method is essentially based on imposing target spatial and temporal correlations on random fields via explicit filtering. The appropriately correlated and scaled random fields are then added to given target mean fields to generate the instantaneous inflow data. The required knowledge of the target flow is therefore limited to mean flow quantities, auto and cross correlations of their fluctuations, and approximate integral spatio-temporal scales for a given auto-correlation function. Contrary to recycling/re-scaling

\* Corresponding author.

E-mail address: [S.Hickel@tudelft.nl](mailto:S.Hickel@tudelft.nl) (S. Hickel).

methods, digital-filter techniques do not introduce any undesired low-frequency or long-wavelength structures. This is an attractive feature of the digital filter that combined with its straightforward integration in numerical solvers have made the technique a common choice for the simulation of several flows of practical interest [12–16].

Despite being widely adopted, however, the digital filter is still far from being the ideal turbulence generator [3]. An important drawback is the lack of proper phase information of realistic turbulent eddies, which inevitably leads to a finite spatial transient during which physical flow structures develop [17]. The resulting adaptation or induction length, that is, the distance required for turbulence to recover from the modeling errors, depends also on the metric of interest, that is, whether one is primarily interested in realistic mean profiles, or also in pressure fluctuations, Reynolds stresses, etc. [18]. In wall-bounded turbulence, this transient typically manifests as a significant dip in the skin-friction distribution [16], which extends over approximately 5 boundary layer thicknesses and is followed by a spatial transient of approximately 10–20 boundary layer thicknesses until agreement with most reference correlations is attained. As indicated by Wenzel et al. [15] and confirmed by Huang et al. [19], the induction length can be even longer when defined based on the compliance with the von Kármán integral equation. In compressible flows, the spatial transient additionally results in strong pressure disturbances that substantially contaminate the downstream acoustic field [16,20].

In an attempt to mitigate some of the aforementioned deficiencies, different improvements of the digital filter technique have been considered [3]. For instance, Di Mare et al. [21] and Veloudis et al. [22] investigated the effect of spatially varying scales at the inflow plane, instead of constant scales throughout, which led to a better prediction of downstream turbulence profiles. Other strategies involve sponge zones located after the digital filter boundary as means to damp spurious acoustic noise from the non-equilibrium flow [16] or directly forcing the solution towards the expected developed state [23]. More recently, Ceci et al. [18] investigated the effect of suppressing streamwise velocity fluctuations at the inflow plane, which led to a faster relaxation of pressure fluctuations. Interestingly, this counter-intuitive approach did not incur additional penalties in the development of the Reynolds stresses, at least in the low supersonic regime.

Therefore, much potential exists for improving the capabilities of the digital filter method. However, proposed improvements have not been investigated systematically and they appear scattered over different studies (which involve different applications, flow conditions and numerical strategies). This makes it hard for researchers to assess, based on an acceptable level of accuracy, whether any additional modifications of the digital filter technique are worth the extra effort. Furthermore, few studies attempt to explain the observed deficiencies from a flow physics perspective, which, in our opinion, is key for further refinement of the method.

The purpose of this paper is thus to systematically assess the efficacy of several methods that can improve the accuracy and performance of the digital filter technique based on a compressible turbulent boundary layer benchmark and to explain the observed differences upon inspection of the dominant terms in the transport equations for the Reynolds stresses. Improvements of accuracy motivated by flow physics include a novel filter kernel function for the transversal directions and varying target length scales with wall-distance. Following a recent suggestion of Ceci et al. [18], we also consider suppressing streamwise velocity fluctuations at the inflow plane. To further improve the latter method, we assess the potential benefits of preserving the inflow turbulence kinetic energy by amplifying one of the cross-stream Reynolds stresses. In addition, we present selected details of our implementation for massively parallel simulations that reduce the computational cost of digital filter turbulent inflow generation methods.

The paper is organized as follows. In Section 2 we briefly describe the baseline digital filter method as well as the considered modifications. Details of the numerical method and the study case are then

provided in Section 3. In Section 4 we present and analyze the results of seven wall-resolved LES with the investigated inflow settings and explain the observed differences based on Reynolds stress budgets. The paper is finally concluded in Section 5 along with further remarks.

## 2. The digital filter method

### 2.1. Baseline method

The baseline digital filter method considered in this paper is based on the method proposed by Xie and Castro [11] for incompressible flows, which is an extension of the original work of Klein et al. [9] and proceeds as follows:

1. At every time step, three slices of uncorrelated Gaussian random numbers  $S_i$ , with  $i = \{1, 2, 3\}$ , are generated. Each slice has zero mean and unit variance, and is uncorrelated from the others.
2. A two-dimensional spatial filter is then applied to each random slice in order to impose spatial coherence. The two-dimensional filter kernel is defined as the tensor product of two one-dimensional kernels that are based on the following exponential correlation function

$$R(r) = \exp\left(-\frac{\pi r}{2I_L}\right), \quad (1)$$

where  $I_L$  is the target integral length scale, which can have different values for each random field, direction, and wall distance. In discrete form, and for a constant grid spacing  $h$  with  $I_L = nh$  and  $r = kh$ , Eq. (1) becomes

$$R(kh) = \exp(-\pi|k|/(2n)). \quad (2)$$

To approximate the discrete filter coefficients, namely  $b_k$ , Xie and Castro [11] propose the following relations

$$b_k = \tilde{b}_k \left( \sum_{j=-N}^N \tilde{b}_j^2 \right)^{-1/2}, \quad \text{and} \quad \tilde{b}_k \approx \exp\left(-\frac{\pi|k|}{n}\right), \quad (3)$$

where  $N$  is the filter support, taken as  $N \geq 2n$ . The spatially filtered fields are denoted as  $\tilde{S}_i$ .

3. Temporal coherence is also assumed of exponential form, and is achieved via

$$\tilde{g}_i(t) = \tilde{g}_i(t - \Delta t) \exp\left(-\frac{\pi \Delta t}{2I_T}\right) + \tilde{S}_i(t) \left[ 1 - \exp\left(-\frac{\pi \Delta t}{I_T}\right) \right]^{1/2}, \quad (4)$$

where  $I_T$  is the target time scale and  $\tilde{g}_i$  are the space-time correlated random fields.

4. The inflow data  $\tilde{u}_i(t) = \tilde{U}_i + u_i''(t)$  is composed of target mean velocity  $\tilde{U}_i$  and instantaneous fluctuations  $u_i''(t) = a_{ij} \tilde{g}_j(t)$ , where  $a_{ij}$  is the Cholesky decomposition of the target Reynolds stress tensor. This transformation, originally proposed by Lund et al. [6], scales the slice variance (originally unity) to provide the target second-order statistics.

We refer the reader to the original publications [9,11] for additional details.

### 2.2. Implementation for compressible flows

For compressible simulations, thermodynamic fluctuations are also required at the inflow boundary. As commonly done in previous works [12], we use the strong Reynolds analogy (SRA) to relate velocity and temperature fluctuations of a perfect gas

$$T'' = -\frac{\tilde{U}_1}{c_p} u_1'', \quad (5)$$

where  $u_1''$  is the streamwise velocity fluctuation given by the digital filter. The mean streamwise velocity  $\tilde{U}_1$  and the specific heat at constant

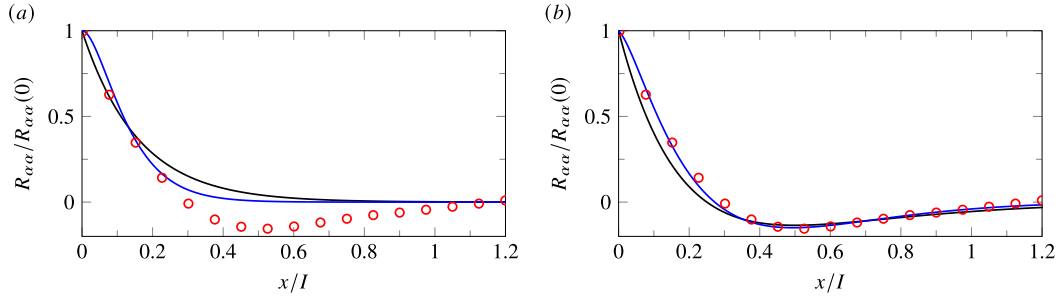


Fig. 1. (a) Exponential correlation suggested by Xie and Castro [11], and (b) proposed correlation function for transversal directions. Black lines target correlation; blue lines: correlation provided by the approximated digital filter kernel; red markers: spanwise  $u'$  auto-correlation function computed from DNS data of a supersonic TBL at Mach 2.0 and  $y/\delta = 0.5$  (from Pirozzoli and Bernardini [25]).

pressure  $c_p$  are inputs. Density and temperature fluctuations are then related through the perfect gas law at constant pressure

$$\rho' = -\frac{\bar{\rho}}{\bar{T}} T'' . \quad (6)$$

The mean density  $\bar{\rho}$  and the mean temperature  $\bar{T}$  are also provided as input. Note that this method approximates an inflow state with zero pressure fluctuations.

All inflow conditions generated by the digital filter are then prescribed at the inflow plane via a characteristic-based method in order to minimize spurious noise [24].

### 2.3. Improvements of accuracy

Xie and Castro [11] propose the exponential form (1) for the velocity correlation function. However, an exponential function is a very poor approximation for the transversal velocity correlation functions in turbulent boundary layers [25], even when optimized length scales are employed. For this reason, we consider a correlation function of the form

$$R(r) = \left(1 - \frac{r}{I_L}\right) \exp\left(-\frac{r}{I_L}\right), \quad (7)$$

which includes negative values and thus much better resembles transversal correlation functions. We propose the following relation

$$\tilde{b}_k \approx \left(1 - \left(\frac{|k|}{n}\right)^{0.3}\right) \exp\left(-\frac{|k|}{n}\right), \quad (8)$$

for the calculation of the discrete filter coefficients in the transversal directions (e.g. for the spanwise coherence of  $u''$ ), which approximates the target transversal correlation function (7) well. In normal directions (e.g., for the spanwise coherence of  $w''$ ), the exponential correlation function proposed by Xie and Castro [11] is still employed since it is a good approximation of the target spatial coherence [26].

Fig. 1 compares the exponential correlation suggested by Xie and Castro [11], in Fig. 1(a), with the correlation function that we propose for the transversal directions, see Fig. 1(b). Black lines denote the corresponding target correlation functions whereas the actual correlations provided by the digital filter with approximated filter coefficients is indicated with a blue line. The length scale is set to  $I_z = 0.25\delta$ , which is the value reported by Pirozzoli and Bernardini [25] for the auto-correlation of  $u'$  in spanwise direction at  $y/\delta = 0.5$  (see figure 26(b) in their publication). The auto-correlation function that Pirozzoli and Bernardini [25] obtain is also included for reference in Fig. 1, which shows that our model correlation (7) for tangential directions as well as the actual correlation provided by digital filter with the approximated filter kernels (8) are in much better agreement with the reference data than the purely exponential relations suggested by Xie and Castro [11].

As means to further increase the accuracy of the inflow data, we employ the zonal approach proposed by Veloudis et al. [22] whereby the digital filter inflow plane is divided in multiple zones with different target scales. The considered zones and their corresponding scales are presented in Section 3.

In addition to modifications that are directly motivated by improving the physical realism of the imposed velocity fluctuations, we also analyze a modification recently proposed by Ceci et al. [18], who found that suppressing streamwise velocity fluctuations at the inflow plane effectively reduces spurious pressure perturbations. Since the inflow turbulence kinetic energy  $k_{in} = \overline{u''_i u''_i} / 2$  would be highly reduced by setting  $u''_1 = 0$ , the potential benefits of preserving  $k_{in}$  by amplifying one of the cross-stream Reynolds stresses is also assessed; that is, we prescribe for the wall-normal stress  $\overline{u''_2 u''_2}(y) = 2k_{in}(y) - \overline{u''_3 u''_3}(y)$  while the spanwise stress  $\overline{u''_3 u''_3}(y)$  remains unaltered, and vice-versa.

Lastly, since pressure fluctuations are an important element in turbulent flows [27,28], we also considered generating both pressure and density fluctuations from the temperature field under the assumption of isentropic flow. For a calorically perfect gas, the isentropic condition implies that  $\rho \propto T^{1/(\gamma-1)}$  which leads to

$$\frac{\rho'}{\bar{\rho}} = \left(1 + \frac{T''}{\bar{T}}\right)^{\frac{1}{\gamma-1}} - 1, \quad (9)$$

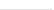






and the corresponding pressure fluctuation then follows from the ideal gas law. Results for this approach, however, are not reported in this paper since no significant changes of the results were observed compared to the SRA-based method, where pressure fluctuations are neglected. This comes as no surprise considering the non-isentropic nature of the thermodynamic fluctuations in compressible turbulent boundary layer flows [26].

### 2.4. Improvements of performance

We refer the reader to Kempf et al. [29] for an efficient baseline implementation of the digital filter method. In this section, we briefly discuss additional performance improvements.

The generation of high-quality random fields can be a major contribution to the computational cost. We have therefore implemented a highly optimized, parallel version of the Mersenne Twister MT19937 of Matsumoto and Nishimura [30] for the generation of single-precision Gaussian random numbers. The compute load is equally distributed over all processes, and each process initializes its random stream at a different position along the sequence. The very long period of the stream avoids unwanted correlations for all practical purposes. Particular attention was put on optimizing memory alignment and vectorization. All operations on the random fields and velocity fluctuations are performed in single precision and only the final inflow data is stored in double precision.

**Table 1**  
Details of the investigated digital filter modifications.

Case	#Zones	$R_t$	update interval	$u''_{in}$ suppressed	$k_{in}$ preserved	$Re_\tau$ at $x^+ = 40$ .	Legend
R0	3	$\exp(-\pi r/(2I_L))$	Every step	No	Yes	1310	
A1	3	$(1-r/I_L) \exp(-r/I_L)$	Every step	No	Yes	1301	
A2	3	$(1-r/I_L) \exp(-r/I_L)$	Every 25 steps	No	Yes	1292	
A3	1	$(1-r/I_L) \exp(-r/I_L)$	Every step	No	Yes	1329	
B1	3	$(1-r/I_L) \exp(-r/I_L)$	Every step	Yes	Yes, via $\overline{u'^2}$	1300	
B2	3	$(1-r/I_L) \exp(-r/I_L)$	Every step	Yes	Yes, via $\overline{w'^2}$	1298	
B3	3	$(1-r/I_L) \exp(-r/I_L)$	Every step	Yes	No	1218	

**Table 2**  
Target length scales per zone, velocity component and spatial direction.

Zone	Range	$L_{ref}$	$I_x/L_{ref}$			$I_y/L_{ref}$			$I_z/L_{ref}$		
			$u$	$v$	$w$	$u$	$v$	$w$	$u$	$v$	$w$
1	0 to $y^+ = 100$	$l_{in}^+$	400	100	60	75	100	50	100	50	100
2	$y^+ = 100$ to $0.2\delta_{0,in}$	$\delta_{0,in}$	1.2	0.2	0.3	0.2	0.2	0.15	0.2	0.15	0.3
3	Above $0.2\delta_{0,in}$	$\delta_{0,in}$	0.9	0.3	0.3	0.3	0.3	0.25	0.35	0.25	0.35

In order to further reduce the computational costs incurred by the method, we update the inflow data at a prescribed time interval instead of every time step. We propose to choose the update interval as  $1/20^{th}$  of the smallest time scale of the input dataset, which for the considered benchmark case corresponds to approximately 25 time-steps. At the intermediate time-steps, linear interpolation is used between the corresponding digital filter solutions. With these measures, the computational cost of the digital filter boundary condition does not significantly affect the load balance of massively parallel simulations and amounts to about 1% of the total wall-clock time.

### 3. Benchmark case and numerical setup

The benchmark case is a zero-pressure-gradient turbulent boundary layer at Mach 2.0 [26]. Stagnation temperature and pressure are set to  $T_0 = 288$  K and  $p_0 = 356$  kPa respectively, and the free-stream flow velocity is  $u_\infty = 507$  m/s. At the inflow plane, the 99% velocity-based boundary layer thickness  $\delta_{0,in}$  is 5.2 mm and the corresponding friction Reynolds number is  $Re_{\tau,in} = 935$ . The fluid is air with a specific heat capacity ratio of  $\gamma = 1.4$  and the specific gas constant  $\mathcal{R} = 287.05$  J(kgK)<sup>-1</sup>. The temperature dependency of the dynamic viscosity is modeled through Sutherland's law and the heat flux is given by Fourier's law. The thermal conductivity is proportional to the dynamic viscosity with a molecular Prandtl number of  $Pr = 0.72$ .

Table 1 includes a summary of the performed simulations and their corresponding digital filter settings. The reference case R0, corresponding to the standard digital filter implementation for compressible flows, considers exponential correlations in all directions. All cases except for A3 consider three different zones at the inflow plane, corresponding to the inner region, the overlap region, and the outer region of the boundary layer. The target length scales, which differ for each zone, are given in Table 2. Case A3, on the other hand, only includes one zone with target length scales corresponding to the largest values in Table 2 per direction and velocity component. Table 1 also states the employed correlation function in tangential directions ( $R_t$ ) and the time-step interval at which new inflow data is generated. For cases B1 to B3 streamwise velocity fluctuations are suppressed at the inflow plane, and additional information is provided regarding the treatment of the turbulence kinetic energy at the inflow  $k_{in}$ . For later reference, the employed line legend in the upcoming figures is also included in Table 1.

The computational domain is a rectangular box with dimensions  $L_x = 45\delta_{0,in}$  (streamwise),  $L_y = 16.5\delta_{0,in}$  (wall-normal), and  $L_z = 4\delta_{0,in}$  (spanwise). The domain is discretized with  $56 \times 10^6$  cells, and the grid spacing in viscous units at the wall is  $\Delta x^+ = 39$ ,  $\Delta y^+ = 0.94$  and  $\Delta z^+ = 9.74$ . Non-reflecting boundary conditions are used at the top and outflow boundaries [24], and periodicity is enforced

in the spanwise direction. The wall is modeled as isothermal at the stagnation temperature, i.e.,  $T_{wall} = T_0$ , and inflow data is generated via the different digital filter methods explained above. For this work, prescribed mean profiles and Reynolds stresses at the inflow plane are adapted from the reference DNS data of Pirozzoli and Bernardini [25].

All simulations are performed with the finite volume solver INCA (<https://www.inca-cfd.com>), which employs the adaptive local deconvolution method (ALDM) for implicit LES of the compressible Navier–Stokes equations [31]. ALDM is a nonlinear solution-adaptive finite volume method that exploits the discretization of the convective fluxes to introduce a physically consistent sub-grid scale turbulence model. Since unresolved turbulence and shock waves require fundamentally different modeling, ALDM relies on a shock sensor to control model parameters. This guarantees the accurate propagation of smooth waves and turbulence without excessive numerical dissipation while providing essentially non-oscillatory solutions at strong discontinuities. Diffusive fluxes are approximated by second-order schemes and a third-order total variation diminishing Runge–Kutta scheme is employed for time integration. The reader is referred to Hickel et al. [31] for implementation details of the method and validation results.

Each simulation proceeded as follows: First, an initial transient of 10 flow-through times (FTT) of the full domain length was simulated to ensure a fully developed turbulent flow in statistical equilibrium. This solution interval was discarded from the analysis. After this transient, simulations were integrated for another 12 FTT of the full domain length. During this second interval, statistics samples were collected at a sampling interval of  $\Delta t u_\infty / \delta_{0,in} \approx 0.013$  and averaged in the homogeneous spanwise direction and in time.

### 4. Results and discussion

In wall-bounded flows, a primary metric to assess the performance of inflow turbulence generators is the evolution of the skin-friction coefficient. This is shown in Fig. 2(a) against the streamwise coordinate  $x^* = (x - x_{in}) / \delta_{0,in}$ , where  $x_{in}$  is the location of the inflow plane. As observed, all cases exhibit a characteristic dip in  $\langle c_f \rangle$  right after the inflow that is recovered within approximately  $5\delta_{0,in}$ . The strength of the dip clearly depends on the digital filter settings; for instance case B1 additionally exhibits an initial overshoot. See Table 1 for details on the employed digital filter settings per simulation as well as the line legend.

While an apparent equilibrium behavior is observed after the transient region of  $5\delta_{0,in}$ , differences between the skin-friction distributions remain visible for the investigated cases. For instance, the  $\langle c_f \rangle$  distributions for cases A1 and A2 are very similar to that for the baseline case R0, while case A3 shows discrepancies that include larger skin-friction magnitudes. This suggests a non-negligible effect of the excessively

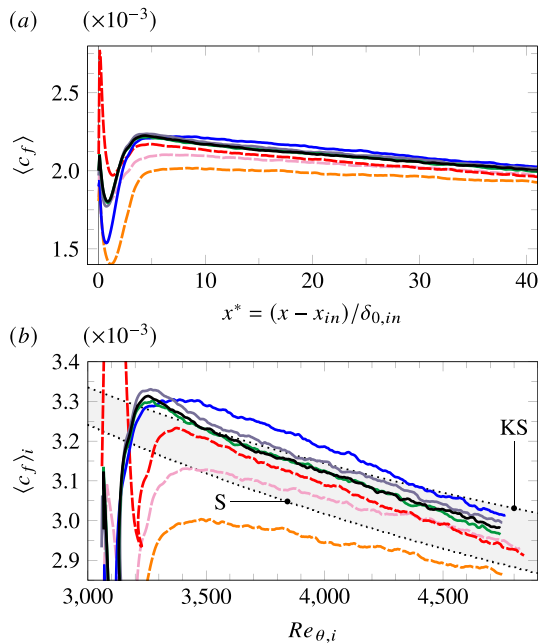


**Fig. 2.** (a) Streamwise evolution of the time- and spanwise-averaged skin-friction, and (b) equivalent incompressible skin-friction as a function of the transformed momentum-thickness Reynolds number. The gray area in (b) is bounded by the correlation of Kármán-Schoenherr [32] (KS) and the correlation of Smits et al. [33] (S). See Table 1 for the line legend and details on the employed digital filter settings per simulation.

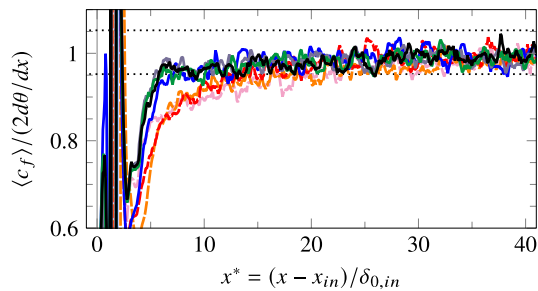


**Fig. 3.** Compliance with the von Kármán integral equation. Dotted lines indicate  $\pm 5\%$  deviation.

large scales at the wall, which is retained throughout the computational domain. Suppressing streamwise velocity fluctuations at the inflow also influences the solution noticeably, with case B3 exhibiting the lowest  $\langle c_f \rangle$  values. Note that  $k_{in}$  is not preserved for case B3.

The van Driest II transformation [34] is employed to remove Mach number effects and enable comparison with reference incompressible correlations. Skin-friction and momentum thickness Reynolds number  $Re_\theta$  are thus reduced to their incompressible counterparts by applying the following transformation

$$c_{f,i} = F_c c_f, \quad Re_{\theta,i} = \frac{\mu_\infty}{\mu_w} Re_\theta. \quad (10)$$

where  $F_c$  is a function of the wall temperature  $T_w$  and nominal adiabatic wall temperature [35]. Resulting distributions are shown in Fig. 2(b) together with the empirical correlation functions of Kármán-Schoenherr [32] (denoted by KS) and of Smits et al. [33] (denoted by S). Combined, these correlations indicate a range of plausible solutions, which appears shaded in gray in the figure. In agreement with the previous discussion, cases A3 and B3 noticeably deviate from the expected behavior. The same can be said for case B2, which only recovers the expected skin-friction distribution at high values of  $Re_{\theta,i}$ , i.e., in the vicinity of the outflow plane. On the other hand, cases R0, A1, A2

and B1 seem to recover the modeling errors faster and exhibit quasi-equilibrium behavior from  $Re_{\theta,i} \approx 3400$  onward. The fact that case B1 is in very good agreement with the reference correlations, while cases B2 and particularly B3 deviate substantially from them, highlights the beneficial effect of preserving the target  $k_{in}$  by amplifying  $v''^2$ . This is expected since the wall-normal stress, as opposed to  $w''^2$ , plays a key role in the turbulence regeneration cycle [36]. We also note that the marginal differences between cases A1 and A2 suggest that spurious interpolation errors do not seem to meaningfully alter the near-wall turbulence development.

In order to better identify the fraction of the computational domain where turbulence is fully established, we also inspect the compliance with the von Kármán integral equation [15,37], i.e.,

$$\langle c_f \rangle = 2 \frac{d\theta}{dx} \quad (11)$$

which relates the growth of the momentum thickness to the local skin-friction coefficient. Note that the above formulation neglects the integral contribution of the Reynolds stresses, as their streamwise derivatives are supposed to contribute negligibly in a fully developed equilibrium boundary layer. This approximation naturally does not hold in the initial transient region, where turbulence is rapidly recovering from modeling errors. An effective compliance evaluator is thus the ratio  $\langle c_f \rangle / (2d\theta/dx)$ , which should approach unity as the boundary layer returns to an equilibrium state.

The streamwise evolution of this parameter is shown for all cases in Fig. 3 together with a  $\pm 5\%$  tolerance band. Despite the residual noise, two clear trends can be observed. On the one hand, the baseline case R0 and cases A1 to A3 satisfy Eq. (11) within 5% accuracy after a transient of about  $5\delta_{0,in}$  from the inflow plane. On the other hand, cases B1 to B3 (in which  $u''$  is suppressed at the inflow) reach the same level of accuracy only  $\sim 10\delta_{0,in}$  from the inflow plane, which is effectively double the distance. Therefore, based on the compliance with the von Kármán integral equation, the nonphysical suppression of streamwise velocity fluctuations at the inflow plane results in a longer adaptation length.

Next, we assess the effect of the considered digital filter modifications on the wall-pressure fluctuations. As these fluctuations are influenced by inner and outer layer eddies [38], they provide a good indication of the overall boundary layer development. The spanwise evolution of the wall-pressure fluctuations is shown in Fig. 4(a). It is evident that all cases systematically over-predict the pressure fluctuations near the inflow. Suppressing streamwise velocity fluctuations has a clear benefit according to this metric. Cases B1 to B3 exhibit the fastest relaxation of the wall-pressure fluctuations. The method proposed by Ceci et al. [18], employed in case B3, predicts the lowest fluctuation intensities. The baseline case R0 and cases A1 to A3, on the other hand, show a slower recovery from the increased wall-pressure fluctuations at the inflow plane. Also note that case A3, the only case that considers exponential correlation functions in all directions and velocity components, results in the largest fluctuation intensities throughout the computational domain.

Empirical evidence suggests a logarithmic  $Re_\tau$ -dependence of the wall-pressure fluctuations when normalized using inner variables, i.e., the wall shear stress  $\tau_w$  [28,38]. To verify whether that is also the case in our LES data, we compare the corresponding inner-scaled wall-pressure fluctuations against the empirical correlation of Farabee and Casarella [39]. This comparison is shown in Fig. 4(b). In agreement with the observations discussed above, cases B1 and B3 closely follow the expected behavior after the initial transient. This is not the case for the baseline case R0 and cases A1 to A3, which seem to asymptotically approach the reference correlation but exhibit larger fluctuations intensities throughout the computational domain. Nevertheless, cases A1 and A2 with our custom transversal correlation function perform better than the baseline case R0 and case A3. The very close agreement of the results for A1 and A2 further justifies updating inflow data at prescribed time intervals to reduce computational costs.

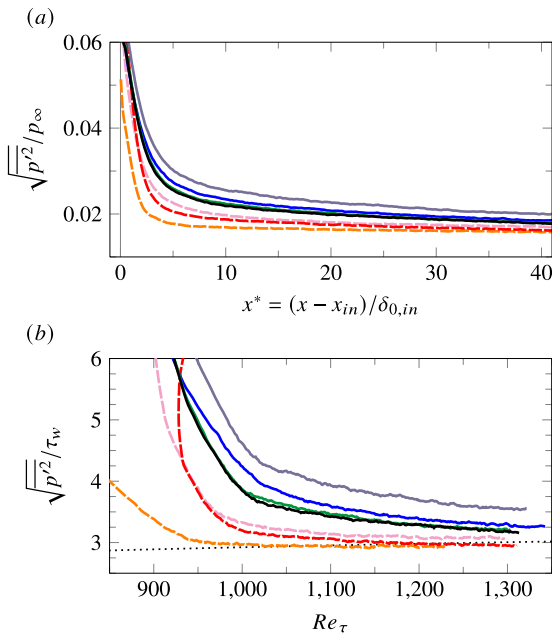


Fig. 4. (a) Streamwise evolution of the time- and spanwise-averaged wall-pressure fluctuations, and (b) inner-scaled wall-pressure fluctuations as a function of the friction Reynolds number. The dotted line indicates the semi-empirical correlation of Farabee and Casarella [39].

We now turn our attention to the evaluation of the Reynolds stresses. First, the evolution of the peak values for the streamwise and shear stresses are considered. The former is indicative of the near-wall streaks, which make up the stress-producing cycle that sustains turbulence [36]. The peak shear stress, on the other hand, is associated with quasi-logarithmic behavior of the mean velocity profile and reflects a multi-scale momentum transfer [40,41]. The streamwise evolution of the inner-scaled streamwise stress peak is shown in Fig. 5(a) for all cases. As observed, the corresponding distributions for the baseline case R0 as well as cases A1, A2, B1 and B2 effectively yield identical values after  $10\delta_{0,in}$  from the inflow plane. Furthermore, these distributions closely follow the empirical relation of Ceci et al. [18] derived from their DNS data, which relates the peak streamwise stress magnitude with the friction Reynolds number (not shown here). The peak streamwise stress for case B3, in turn, shows a much slower recovery as indicated by the dashed orange line in Fig. 5(a). This further highlights the importance of preserving the turbulence kinetic energy at the inflow plane, which did not happen for this case. Therefore, our results indicate that suppressing  $u''$  can meaningfully hamper the near-wall turbulence development when the inflow turbulence is energy deficient. Fig. 5(b) shows that the evolution of the inner-scaled peak magnitude of the Reynolds shear stress is less affected by the inflow conditions than the peak magnitude of  $\overline{u''u''}$ . As observed, all cases exhibit a constant peak value close to unity after approximately  $10-15\delta_{0,in}$  from the inflow plane. However, cases A1, A2 and B1 exhibit a faster development than the other cases, with an adaptation length of approximately  $7\delta_{0,in}$  for this metric.

To this end, conclusions can be drawn about the analysis of the results so far. By comparing the data for cases A1 and A2, it is clear that updating the inflow data at a prescribed time interval does not incur additional penalties, and is therefore desired performance-wise. The addition of multiple inflow zones with varying length scales per zone, as done for all cases except for case A3, is also recommended as it leads to a faster relaxation of the local skin-friction and peak magnitudes of the inner-scaled Reynolds stresses, see Fig. 2 and Fig. 5 respectively. The alternative correlation function for the transversal directions defined in Eq. (7) leads to a substantial reduction of the

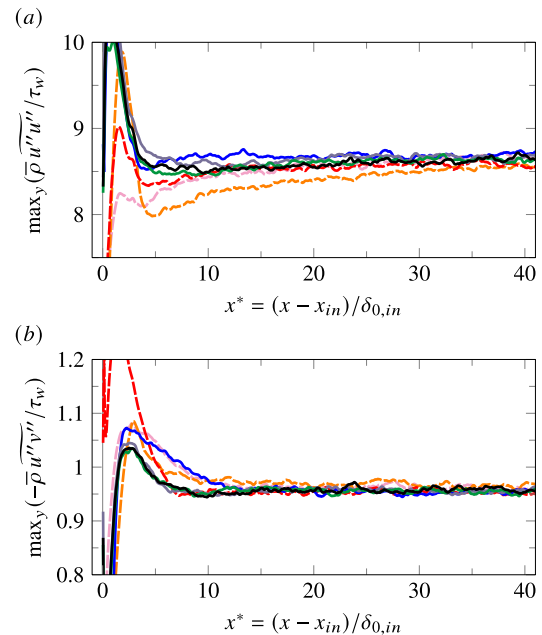


Fig. 5. Streamwise evolution of normalized Reynolds stresses: (a) streamwise stress, and (b) shear stress.

spurious acoustic radiation of the non-equilibrium boundary layer and small improvements for the other metrics. However, if the downstream acoustic field is a priority, suppressing streamwise velocity fluctuations at the inflow plane becomes appealing as it leads to the fastest relaxation of the wall-pressure fluctuation intensity, see Fig. 4. Provided that sufficient energy is supplied by amplifying the wall-normal Reynolds stress  $v''^2$ , our results indicate that the only deficiency of this approach, at least in a qualitative sense, is the poor compliance with the von Kármán integral equation within the first  $10\delta_{0,in}$  from the inflow plane.

The question now remains as to what physical mechanisms contribute to a longer adaptation length, and why suppressing streamwise velocity fluctuations at the inflow plane leads to a rapid turbulence development and a quieter downstream flow. To shed some light on these matters, the two-dimensional distributions of the primary Reynolds stresses (i.e., streamwise, wall-normal and shear) and their transport budgets are examined. The former are shown in Fig. 6 for cases A1 and B1 near the digital filter boundary to highlight the near-inflow behavior. The streamwise stress fields shown in Figs. 6(a) and 6(d) exhibit the expected differences, i.e., the stress is mostly convected downstream from the inflow plane for case A1 while it is rapidly generated for case B1. As indicated in Fig. 5(a), both distributions converge to the same peak  $u''^2$  magnitude within  $\sim 10\delta_{0,in}$  from the digital filter boundary. With respect to the other stresses,  $-u''v''$  and  $v''^2$ , interesting observations can be made for case A1. As observed in Figs. 6(b) and 6(c), both stresses initially fall noticeably below the target magnitude for this case, and they progressively recover within  $\sim 3\delta_{0,in}$  from the inflow plane. The baseline case R0 as well as cases A2 and A3 also exhibit the exact same behavior near the inflow (not shown here), indicating that this is a characteristic drawback associated with the baseline digital filter implementation for compressible flows. The wall-normal stress for case B1, on the other hand, initially decays but does not significantly undershoot the target value, see Fig. 6(f). Therefore, the deliberate amplification of this stress at the digital filter boundary gives superior results during the initial transient. In addition, and similarly to the streamwise stress, the shear stress for this case is also rapidly generated, see Fig. 6(e).

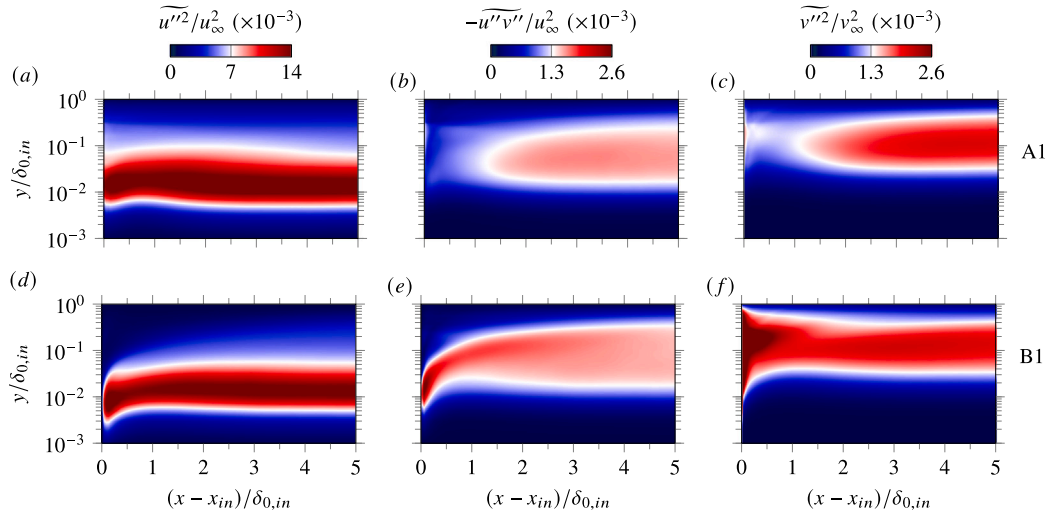


Fig. 6. Streamwise stress, shear stress and wall-normal stress distributions for (a)–(c) case A1, and (d)–(f) case B1.

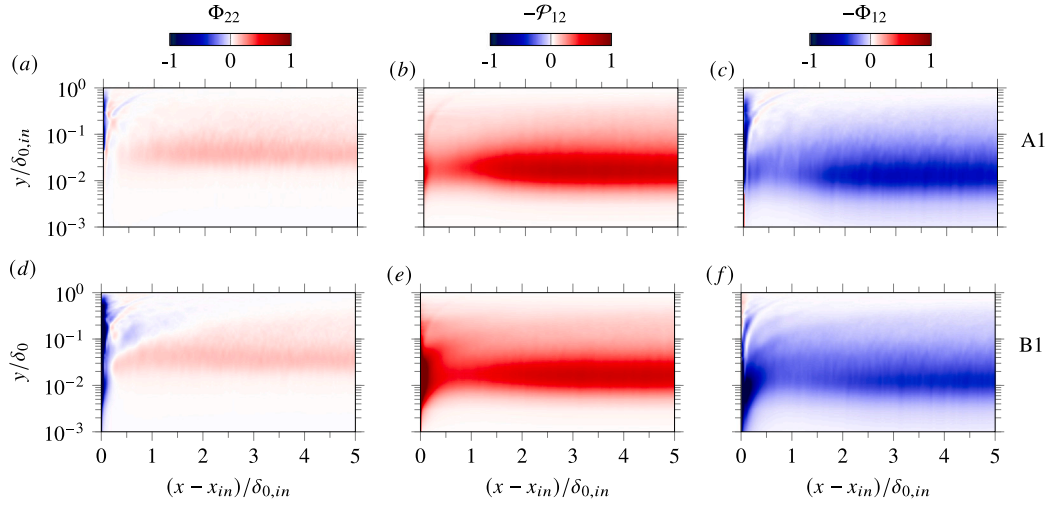


Fig. 7. Pressure-gradient/velocity correlation terms  $\Phi_{22}$  and  $-\Phi_{12}$ , and shear stress production  $-\mathcal{P}_{12}$  for (a)–(c) case A1, and (d)–(f) case B1. All terms are normalized with  $u_\infty^3/\delta_{0,in}$ .

The observed behavior near the inflow can be explained by inspecting the dominant terms in the transport equations for the  $\overline{u''v''}$  and  $\overline{v''^2}$  Reynolds stresses. In convective form, the transport equation for  $u''_i u''_j$  reads

$$\frac{\partial \overline{u''_i u''_j}}{\partial t} + \tilde{u}_k \frac{\partial \overline{u''_i u''_j}}{\partial x_k} = \mathcal{P}_{ij} + D_{ij} + \Pi_{ij} + \mathcal{M}_{ij} - \epsilon_{ij} \quad (12)$$

where  $\mathcal{P}_{ij}$  is production ( $-\tau_{ik} \partial_{x_k} \tilde{u}_j - \tau_{jk} \partial_{x_k} \tilde{u}_i$ ),  $D_{ij} = D_{ij}^v + D_{ij}^T + D_{ij}^p$  is the transport term that comprises viscous diffusion  $\bar{\rho} D_{ij}^v$  ( $\partial_{x_k} [\sigma'_{ik} u''_j + \sigma'_{jk} u''_i]$ ), turbulent convection  $\bar{\rho} D_{ij}^T$  ( $-\partial_{x_k} [\rho u''_i u''_j u''_k]$ ) and pressure transport  $\bar{\rho} D_{ij}^p$  ( $-\partial_{x_k} [\overline{p' u''_i \delta_{jk}} + \overline{p' u''_j \delta_{ik}}]$ ),  $\bar{\rho} \Pi_{ij}$  is the pressure-strain correlation ( $\overline{p'(u''_{j,i} + u''_{i,j})}$ ),  $\bar{\rho} \epsilon_{ij}$  is dissipation ( $\overline{\sigma'_{ik} u''_{j,k} + \sigma'_{jk} u''_{i,k}}$ ) and  $\bar{\rho} \mathcal{M}_{ij}$  the turbulent mass flux ( $u''_i (\partial_{x_k} \bar{\sigma}_{jk} - \partial_{x_j} \bar{p}) + u''_j (\partial_{x_k} \bar{\sigma}_{ik} - \partial_{x_i} \bar{p})$ ) [42].

Starting with the wall-normal stress, we find that the terms that contribute most to its initial decay are those involving the pressure, that is, the pressure transport and pressure-strain correlation terms. For the sake of simplicity, we consider their aggregate effect via the pressure-gradient/velocity correlation term  $\Phi_{ij} = D_{ij}^p + \Pi_{ij}$ . The corresponding contribution to the balance of  $\overline{v''^2}$ , i.e.,  $\Phi_{22}$ , is thus shown for cases A1 and B1 in Figs. 7(a) and 7(d), respectively. As observed,  $\Phi_{22}$  constitutes a sink near the inflow plane in both cases, whereas this term is supposed to be the major source of energy for  $\overline{v''^2}$  in an equilibrium boundary

layer (there is no direct contribution from production, [42]). This could be expected for case B1, since the pressure-strain correlation may be redistributing the energy from the deliberately amplified  $\overline{v''^2}$  to the other stresses. However,  $\Phi_{22}$  becoming a sink for case A1 represents an important weakness of the digital filter technique; it fails to realistically account for this term.

Since the production term for  $-\overline{u''v''}$ , namely  $\mathcal{P}_{12}$ , is directly proportional to  $\overline{v''^2}$ , variations in the latter directly impact the shear stress balance. The production term for the shear stress is shown in Figs. 7(b) and 7(e) for cases A1 and B1, and confirms this correspondence. For case A1, a decay in  $-\mathcal{P}_{12}$  near the inflow is clearly visible. For case B1, on the other hand, the amplification of  $\overline{v''^2}$  leads to a large  $-\mathcal{P}_{12}$  close to the digital filter boundary that promotes the generation of  $-\overline{u''v''}$  instead, see Fig. 7(e). Since the main energy sink for the shear stress is  $-\Phi_{12}$ , we also show the contributions of this term in Figs. 7(c) and 7(f) for the two cases considered. As observed,  $-\Phi_{12}$  is very strong in magnitude near the inflow in both cases, and this negative contribution extends throughout most of the boundary layer thickness for case A1. Since  $-\Phi_{12}$  exceeds  $-\mathcal{P}_{12}$  at the digital filter boundary for this case,  $-\overline{u''v''}$  is effectively damped as shown in Fig. 6(b). The same cannot be said for case B1, which exhibits a net production of shear stress near the wall. It is also important to note that, while the production term for



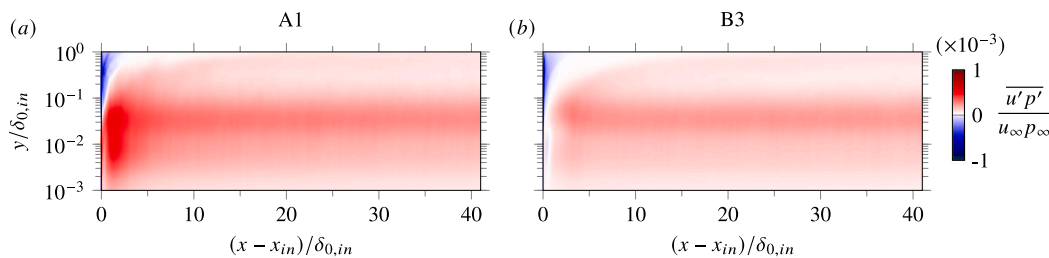


Fig. 8. Normalized pressure–velocity correlation  $\overline{u'p'}$  for (a) case A1, and (b) case B3.

the streamwise stress is directly proportional to  $-u''v''$ , this stress does not exhibit an initial decay at the inflow plane for case A1. In fact, as shown in Fig. 5(a), it is initially amplified and then decays towards the expected value. The reason is that the dissipation and pressure-gradient/velocity correlation terms, which are important in balancing production in the buffer and quasi-logarithmic layers [43], also exhibit reduced values near the inflow. For instance,  $\Phi_{11}$ , which is not shown here, is positive near the wall.

Therefore, it is clear that the inability of the digital filter to realistically account for different terms in the Reynolds-stress transport equation, and in particular those involving the pressure, contributes greatly to the spatial transient. By considering zero pressure fluctuations and the SRA in the digital filter implementation for compressible flows, nonphysical pressure fluctuations are only generated inside the computational domain, and fluctuations observed directly at the inflow are due to the non-reflecting nature of the boundary scheme. These spurious fluctuations disrupt the pressure-related mechanisms in the Reynolds stress transport equation, and consequently, the turbulence regeneration cycle. A further confirmation of this is the fact that employing the above mentioned isentropic assumption to impose non-zero  $p'$  at the inflow does not improve the results, since the fluctuations are still nonphysical. Additionally, we find that the pressure fluctuations that develop near the inflow are directly correlated with  $u''$ , which generally exhibits very large integral scales in streamwise direction. As a consequence, increased fluctuation intensities are retained for a long distance within the computational domain as illustrated in Fig. 4(a) for the baseline case R0 and cases A1–A3. The suppression of the streamwise velocity fluctuations, in turn, effectively eliminates the correlation between  $u''$  and the thermodynamic fluctuations, which leads to a faster relaxation of the latter. The pressure velocity correlation  $\overline{u'p'}$  is shown in Fig. 8 for cases A1 and B3 to illustrate the above-mentioned.

## 5. Conclusions

We have discussed several methods for improving the accuracy and performance of the digital filter turbulent inflow generation technique based on a compressible turbulent boundary layer benchmark and corresponding metrics. A total of 7 wall-resolved large-eddy simulations were carried out to evaluate the efficacy of these methods. We believe that the conclusions reached based on these data equally hold for wall-modeled large-eddy simulations as well as for direct numerical simulations.

Regarding improvements of performance, we propose to update the inflow data at a prescribed time interval based on a turbulent time scale rather than every time-step and to interpolate instantaneous solutions at intermediate time-steps. Results show that this does not incur any penalties, and is therefore a desired modification with strong cost benefits. The studied improvements of accuracy include a novel filter kernel for the transversal directions, varying target length scales with wall-distance, and suppressing streamwise velocity fluctuations at the inflow plane. The proposed correlation function for the transversal directions reduces the nonphysical acoustic radiation during the transient phase and yields small improvements for other metrics. Employing different scales at the inflow plane leads to a reduced adaptation length

in most of the metrics considered, and is also desired. Suppressing streamwise velocity fluctuations at the inflow unambiguously leads to the fastest relaxation of the pressure fluctuations, but also to a longer transient of non-compliance with the von Kármán integral equation. We highlight the benefits of preserving the target turbulence kinetic energy by amplifying the wall-normal Reynolds stresses when the streamwise velocity fluctuations are suppressed.

Our inspection of the compressible Reynolds stress transport equation revealed that the main deficiencies of the digital filter technique are rooted in the pressure-related terms. Nonphysical pressure fluctuation amplitudes and pressure–velocity correlations disrupt the turbulence redistribution and regeneration cycle. Additionally, we find that pressure fluctuations generated near the inflow are spuriously correlated with  $u''$ , and are therefore retained for a long distance downstream of the inflow plane. This explains why an artificial suppression of the streamwise velocity fluctuations, which effectively eliminates this correlation, leads to a faster relaxation of the pressure variance. In view of these results, future attempts towards improving the digital filter technique should aim at modeling pressure fluctuations as well as their correlation with the velocity components.

## Declaration of competing interest

The authors declare that they have no known competing financial interests or personal relationships that could have appeared to influence the work reported in this paper.

## Data availability

Data will be made available on request.

## Acknowledgments

We acknowledge PRACE for awarding us access to HAWK at the High-Performance Computing Center Stuttgart, Germany.

## References

- [1] Tabor GR, Baba-Ahmadi MH. Inlet conditions for large eddy simulation: A review. *Comput & Fluids* 2010;39(4):553–67.
- [2] Wu X. Inflow turbulence generation methods. *Annu Rev Fluid Mech* 2017;49:23–49.
- [3] Dhamankar NS, Blaisdell GA, Lyrantzis AS. Overview of turbulent inflow boundary conditions for large-eddy simulations. *AIAA J* 2018;56(4):1317–34.
- [4] Johansson PS, Andersson HI. Generation of inflow data for inhomogeneous turbulence. *Theor Comput Fluid Dyn* 2004;18(5):371–89.
- [5] Kim J, Lee C. Deep unsupervised learning of turbulence for inflow generation at various Reynolds numbers. *J Comput Phys* 2020;406:109216.
- [6] Lund TS, Wu X, Squires KD. Generation of turbulent inflow data for spatially-developing boundary layer simulations. *J Comput Phys* 1998;140(2):233–58.
- [7] Xu S, Martin MP. Assessment of inflow boundary conditions for compressible turbulent boundary layers. *Phys Fluids* 2004;16(7):2623–39.
- [8] Le H, Moin P, Kim J. Direct numerical simulation of turbulent flow over a backward-facing step. *J Fluid Mech* 1997;330:349–74.
- [9] Klein M, Sadiki A, Janicka J. A digital filter based generation of inflow data for spatially developing direct numerical or large eddy simulations. *J Comput Phys* 2003;186(2):652–65.

- [10] Jarrin N, Benhamadouche S, Laurence D, Prosser R. A synthetic-eddy-method for generating inflow conditions for large-eddy simulations. *Int J Heat Fluid Flow* 2006;27(4):585–93.
- [11] Xie Z-T, Castro IP. Efficient generation of inflow conditions for large eddy simulation of street-scale flows. *Flow Turbul Combust* 2008;81(3):449–70.
- [12] Touber E, Sandham ND. Large-eddy simulation of low-frequency unsteadiness in a turbulent shock-induced separation bubble. *Theor Comput Fluid Dyn* 2009;23(2):79–107.
- [13] Grilli M, Hickel S, Adams NA. Large-eddy simulation of a supersonic turbulent boundary layer over a compression–expansion ramp. *Int J Heat Fluid Flow* 2013;42:79–93.
- [14] Pasquariello V, Hickel S, Adams NA. Unsteady effects of strong shock-wave/boundary-layer interaction at high Reynolds number. *J Fluid Mech* 2017;823:617–57.
- [15] Wenzel C, Selent B, Kloker M, Rist U. DNS of compressible turbulent boundary layers and assessment of data/scaling-law quality. *J Fluid Mech* 2018;842:428–68.
- [16] Adler MC, Gonzalez DR, Stack CM, Gaitonde DV. Synthetic generation of equilibrium boundary layer turbulence from modeled statistics. *Comput & Fluids* 2018;165:127–43.
- [17] Keating A, Piomelli U, Balaras E, Kaltenbach H-J. A priori and a posteriori tests of inflow conditions for large-eddy simulation. *Phys Fluids* 2004;16(12):4696–712.
- [18] Ceci A, Palumbo A, Larsson J, Pirozzoli S. Numerical tripping of high-speed turbulent boundary layers. *Theor Comput Fluid Dyn* 2022;36(6):865–86.
- [19] Huang J, Duan L, Choudhari MM. Direct numerical simulation of hypersonic turbulent boundary layers: Effect of spatial evolution and Reynolds number. *J Fluid Mech* 2022;937:A3.
- [20] Dhamankar NS, Martha CS, Situ Y, Aikens KM, Blaisdell GA, Lyrantzis AS, et al. Digital filter-based turbulent inflow generation for jet aeroacoustics on non-uniform structured grids. *AIAA paper* 2014-1401.
- [21] Di Mare L, Klein M, Jones WP, Janicka J. Synthetic turbulence inflow conditions for large-eddy simulation. *Phys Fluids* 2006;18(2).
- [22] Veloudis I, Yang Z, McGuirk JJ, Page GJ, Spencer A. Novel implementation and assessment of a digital filter based approach for the generation of LES inlet conditions. *Flow Turbul Combust* 2007;79(1):1–24.
- [23] Larsson J. Simple inflow sponge for faster turbulent boundary-layer development. *AIAA J* 2021;59(10):4271–3.
- [24] Poinso T, Lelef SK. Boundary conditions for direct simulations of compressible viscous flows. *J Comput Phys* 1992;101(1):104–29.
- [25] Pirozzoli S, Bernardini M. Turbulence in supersonic boundary layers at moderate Reynolds number. *J Fluid Mech* 2011;688:120–68.
- [26] Laguarda L, Hickel S, Schrijer FFJ, van Oudheusden BW. Assessment of Reynolds number effects in supersonic turbulent boundary layers. *Int J Heat Fluid Flow* 2024;105:109234.
- [27] Tsuji Y, Fransson JH, Alfredsson PH, Johansson AV. Pressure statistics and their scaling in high-Reynolds-number turbulent boundary layers. *J Fluid Mech* 2007;585:1–40.
- [28] Bernardini M, Pirozzoli S. Wall pressure fluctuations beneath supersonic turbulent boundary layers. *Phys Fluids* 2011;23(8):085102.
- [29] Kempf A, Wysocki S, Pettit M. An efficient, parallel low-storage implementation of Klein's turbulence generator for LES and DNS. *Comput & Fluids* 2012;60:58–60.
- [30] Matsumoto M, Nishimura T. Mersenne twister: A 623-dimensionally equidistributed uniform pseudo-random number generator. *ACM Trans Model Comput Simul* 1998;8(1):3–30.
- [31] Hickel S, Egerer CP, Larsson J. Subgrid-scale modeling for implicit large eddy simulation of compressible flows and shock-turbulence interaction. *Phys Fluids* 2014;26(10):106101.
- [32] Hopkins EJ, Inouye M. An evaluation of theories for predicting turbulent skin friction and heat transfer on flat plates at supersonic and hypersonic Mach numbers. *AIAA J*. 1971;9(6):993–1003.
- [33] Smits AJ, Matheson N, Joubert PN. Low-Reynolds-number turbulent boundary layers in zero and favorable pressure gradients. *J Ship Res* 1983;27(03):147–57.
- [34] Van Driest ER. The problem of aerodynamic heating. *Institute of the Aeronautical Sciences*; 1956.
- [35] Shahab MF, Lehnasch G, Gatski TB, Comte P. Statistical characteristics of an isothermal, supersonic developing boundary layer flow from DNS data. *Flow Turbul Combust* 2011;86(3):369–97.
- [36] Panton RL. Overview of the self-sustaining mechanisms of wall turbulence. *Prog Aerosp Sci* 2001;37(4):341–83.
- [37] Schlatter P, Örlü R, Li Q, Brethouwer G, Fransson JHM, Johansson AV, et al. Turbulent boundary layers up to  $Re_\theta=2500$  studied through simulation and experiment. *Phys Fluids* 2009;21(5):051702.
- [38] Bull MK. Wall-pressure fluctuations beneath turbulent boundary layers: Some reflections on forty years of research. *J Sound Vib* 1996;190(3):299–315.
- [39] Farabee TM, Casarella MJ. Spectral features of wall pressure fluctuations beneath turbulent boundary layers. *Phys Fluids A: Fluid Dyn* 1991;3(10):2410–20.
- [40] Jiménez J. Cascades in wall-bounded turbulence. *Annu Rev Fluid Mech* 2012;44:27–45.
- [41] Chen X, Hussain F, She Z-S. Non-universal scaling transition of momentum cascade in wall turbulence. *J Fluid Mech* 2019;871.
- [42] Hatay F, Biringen S. Direct numerical simulation of low-Reynolds number supersonic turbulent boundary layers. In: *33rd Aerospace sciences meeting and exhibit*. 1995, p. 581.
- [43] Vyas MA, Yoder DA, Gaitonde DV. Reynolds-stress budgets in an impinging shock-wave/boundary-layer interaction. *AIAA J* 2019;57(11):4698–714.